



Multipolar, polarization-shaped high-order harmonic generation by intense vector beams

Jonas Wätzel and Jamal Berakdar 

Institute for Physics, Martin-Luther-University Halle-Wittenberg, 06099 Halle, Germany

 (Received 19 December 2019; accepted 24 March 2020; published 20 April 2020)

High-order harmonic generation (HHG) is a manifestation of the strongly nonlinear response of matter to intense laser fields and has, as the basis for coherent XUV sources, a variety of applications. Recently, HHG from atoms in a phase and polarization structured laser was demonstrated and interpreted based on the transverse electric-field component of the driving pulse. Here, we point out that as dictated by Maxwell equations, such fields have a longitudinal component which in general has a fundamental influence on the charge dynamics. For instance, its interplay with the transversal field component enables endowing the emitted radiation locally with circular polarization and a defined polarity. It is shown that the time-dependent Stokes parameters defining the polarization state of HHG can be tuned by varying the waist of the driving field, which in turn changes the ratio between the longitudinal and transverse electric-field components of the driving laser. In addition, employing a multipole expansion of the produced harmonics exposes the specific multipolar character and the relation to the spatial structure of the driving field polarization states. The scheme proposed here allows a full polarization control of the emitted harmonics by only one driving laser. A tighter focusing of the driving pulse renders possible the emission of harmonics with both even and odd spatial symmetry. The underlying mechanism is due to the fundamental interplay between the transverse and longitudinal components of the laser's electromagnetic vector potential. The ratio between those components is controllable by just focusing the laser spot, pointing to an accessible tool for polarization and polarity control of the high-order harmonics.

DOI: [10.1103/PhysRevA.101.043409](https://doi.org/10.1103/PhysRevA.101.043409)

I. INTRODUCTION

High-order harmonic generation (HHG) due to highly nonlinear light-matter interactions [1] paved the way for new types of XUV sources and ultrafast (attosecond) spectroscopy [2,3]. In recent years, driving with phase (optical vortices) or polarization structured (vector beams) fields has attracted much attention [4–12], as the driving field characteristics allow one to modulate the properties of the generated harmonics. A particularly interesting driving field is the radially polarized vector beam (RVB). Such RVBs can be tightly focused [13] and are attractive for a number of applications, including ultrafast diffraction [14] or lithography [15,16]. RVBs are in general inherently nontransverse [17] and may have a strong longitudinal electric-field component [18] for a tightly focused beam (cf. Appendix). This property is reflected in a new form of light-matter interaction [19], and hence features in HHG akin to the nontransverse RVB are to be expected, a case not yet clarified. Another key point is that the longitudinal and transversal electric fields $E_{\text{RVB}}^{(\rho)}$ and $E_{\text{RVB}}^{(\rho)}$ oscillate with a phase difference of $\pi/2$. Hence, for a tightly focused RVB, one can find positions in the beam spot with prevalent (local) circular polarization when $E_{\text{RVB}}^{(\rho)}$ and $E_{\text{RVB}}^{(\rho)}$ are of the same magnitude, a fact pointing to a possible polarization shaping of the HHG in a target driven by RVB. Indeed, the results presented here for HHG in a RVB-driven atomic ensemble confirm the fundamental importance of the interplay between the transverse and longitudinal components of RVB, an effect tunable by the laser focusing that changes the ratio between the two component amplitudes. By doing so the circular polarization of HHG and in fact the spatially

dependent Stokes parameters can be tuned. Other effective methods for circularly polarized HHG [20,21] use, for instance, bichromatic elliptically polarized pump beams [22] or counter-rotating few-cycle laser fields [23]. Distinctive features of our HHs are their spatially multipolar character in addition to their polarization states. The symmetries of our HHs are analyzed below using a vectorial multipole expansion. Structures in the spectrum appear due to the transversal (even-symmetry) and the longitudinal (odd-symmetry) components of the driving field. Hence, the focused RVBs provide a frequency-dependent tool for generating odd and even (X)UV harmonics.

II. THEORETICAL MODEL

The vector and the scalar potentials of the harmonics at the detector position r_d which are produced by an elementary (atomic) emitter at the position r_i are inferred from the laser-driven charge (ρ_i) and current (\mathbf{j}_i) density distributions as

$$A_i(\mathbf{r}_d, t) = \mu_0/(4\pi) \int d\mathbf{r}' j_i(\mathbf{r}', t_R)/|\mathbf{r}_d - \mathbf{r}_i - \mathbf{r}'|$$

and

$$\Phi_i(\mathbf{r}_d, t) = 1/(4\pi\epsilon_0) \int d\mathbf{r}' \rho_i(\mathbf{r}', t_R)/|\mathbf{r}_d - \mathbf{r}_i - \mathbf{r}'|,$$

where $t_R = t - |\mathbf{r}_d - \mathbf{r}_i - \mathbf{r}'|/c$ is the retarded time, and r_i is the axial distance to the incident vector-beam optical axis (which sets the z axis of the global coordinate system). $j_i(\mathbf{r}, t)$ and $\rho_i(\mathbf{r}, t)$ of the individual atoms follow from a numerical propagation of the time-dependent

three-dimensional Schrödinger equation [24] involving the time-dependent Hamiltonian (we use atomic units for the quantum dynamics)

$$\hat{H}_i(t) = [\hat{\mathbf{p}} - \mathbf{A}_{\text{RVB}}(\mathbf{r} - \mathbf{r}_i, t)]^2/2 + V(r_i).$$

Here, $\hat{\mathbf{p}}$ is the momentum operator, and we assume the target as a gas of hydrogenic atoms, meaning $V(r) = -1/r$ is the Coulomb potential. The vector potential of RVB is taken as a Bessel mode [19] so that a proper description of the electric longitudinal component is included automatically; using Laguerre-Gaussian modes (cf. Appendix) leads to the same conclusions drawn below. The total vector and scalar potentials at the detector positioned at \mathbf{r}_d are the sum of the vector fields produced by the individual emitters

$$\mathbf{A}(\mathbf{r}_d, t) = \sum_i \mathbf{A}_i(\mathbf{r}_d, t) \quad \text{and} \quad \Phi(\mathbf{r}_d, t) = \sum_i \Phi_i(\mathbf{r}_d, t).$$

The electromagnetic fields read

$$\mathbf{E}(\mathbf{r}_d, t) = -\partial_t \mathbf{A}(\mathbf{r}_d, t) - \nabla_{\mathbf{r}_d} \Phi(\mathbf{r}_d, t)$$

and

$$\mathbf{B}(\mathbf{r}_d, t) = \nabla_{\mathbf{r}_d} \times \mathbf{A}(\mathbf{r}_d, t).$$

We confirmed our scheme is equivalent to using Jefimenko's equations [25,26]. Phase-mismatch effects may arise from dipole phase dependencies on the intensity, Gouy phase variation around the focal plane, and dispersion effects in the neutral gas or in plasma. For optimal phase matching (phase mismatch of the n th harmonic $k_n \rightarrow 0$) the gas jet is placed behind the RVB focal plane [27,28]. Further, our HHG process is carrier-envelope-phase insensitive [29]. To focus on HHG, we assume a low-density target and suppress further discussions of optical refraction and propagation effects.

III. POLARIZATION CONTROL OF HHG

The opening angle α of the Bessel cone sets the spatial extent in the focal plane [cf. Fig. 1(b)] and the ratio between the peak longitudinal (on the optical axis) and transversal components (at the axial distance ρ_{max}). Both components are important for the predicted effects. Increasing α tightens the spot size (meaning ρ_{max} shrinks). The spatial inhomogeneity causes the Stokes parameters to become space dependent. Due to cylindrical symmetry, it is sufficient to investigate the Stokes parameters in the x - z plane with the standard definitions [30]: S_1 and S_2 describe linear polarizations in the directions \hat{e}_x, \hat{e}_z and $(\hat{e}_x \pm \hat{e}_z)/\sqrt{2}$ while S_3 signifies circular polarization in the local plane. Figure 1(c) shows the Poincaré sphere depending on focusing (or on the opening angle α) at an axial distance of $0.5 \mu\text{m}$ with astonishing implications. For a weak focusing ($\alpha = 26^\circ$), we find that the polarization is nearly linear, characterized by $S_1 \approx 1$. Tightening the beam spot moves the Poincaré vector towards the poles, indicating *circular* polarization. Furthermore, the vector always points on the meridian spanned by S_1 and S_3 , signaling that linear polarization in the directions $(\hat{e}_x \pm \hat{e}_z)/\sqrt{2}$ is suppressed. The polarization landscape in the focal plane is rather involved [cf. Fig. 1(d)]: Depending on the axial distance, we find a variation of the polarization state. While around the optical axis (where the longitudinal component dominates) the polarization points

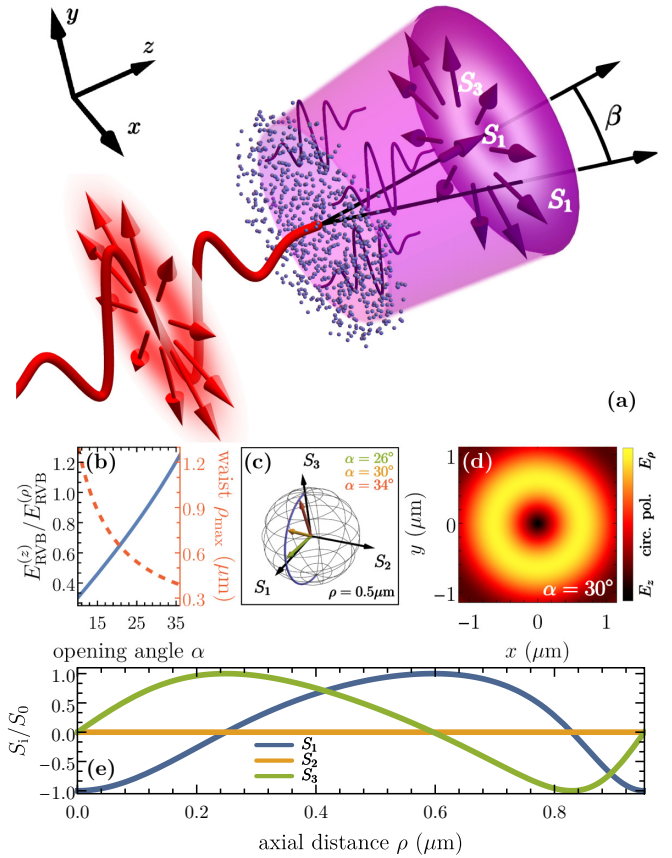


FIG. 1. High-order harmonic generation driven by an intense radially polarized laser. (a) Schematic view of the HHG process: An intense, radially polarized fs IR field is focused on a hydrogenic gas jet that responds with high-order harmonic emission. The radiated field possesses an inhomogeneous distribution of the Stokes parameters $S_{1,2,3}$. (b) Blue curve: Incoming beam opening angle α dependence of the ratio of its on-axis longitudinal component $E_{\text{RVB}}^{(z)}$ to its transverse component $E_{\text{RVB}}^{(\rho)}$ (at ρ_{max}). Beam waist variation is shown by the red curve. (c) Poincaré sphere for different α 's at an axial distance of $0.5 \mu\text{m}$. (d) Color map of polarization landscape in the focal plane $z = 0$ for $\alpha = 30^\circ$. (e) Spatial dependencies of the normalized Stokes parameter S_i/S_0 ($i = 1, 2, 3$) corresponding to RVB with $\alpha = 30^\circ$.

in the z direction (Stokes parameter $S_1 \approx -1$), we find a transition region where $E_{\text{RVB}}^{(\rho)} \approx E_{\text{RVB}}^{(z)}$. The polarization state is circular because both components oscillate with a phase difference of $\pi/2$. Around ρ_{max} , the transversal component dominates, resulting in linear polarization perpendicular to the optical axis, meaning $S_1 \approx +1$. Our strongest focusing (at $\alpha = 35^\circ$) corresponds to a full width at half maximum (FWHM) of $1.2 \mu\text{m}$ which is 1.5λ . Current focusing techniques are capable of generating vector beams with such a tight focus (even subdiffraction focusing is possible) [31].

For illustrations we run numerical simulations employing a four-cycle-long IR (800-nm) radial vector beam with a \sin^2 envelope and with a peak intensity at ρ_{max} fixed at $1.60 \times 10^{14} \text{ W/cm}^2$, independent of opening angle α . The first four panels of Fig. 2 present the angular profiles of the Poynting vector of two chosen harmonics for different focusings of the incident beam. The far-field Poynting vector

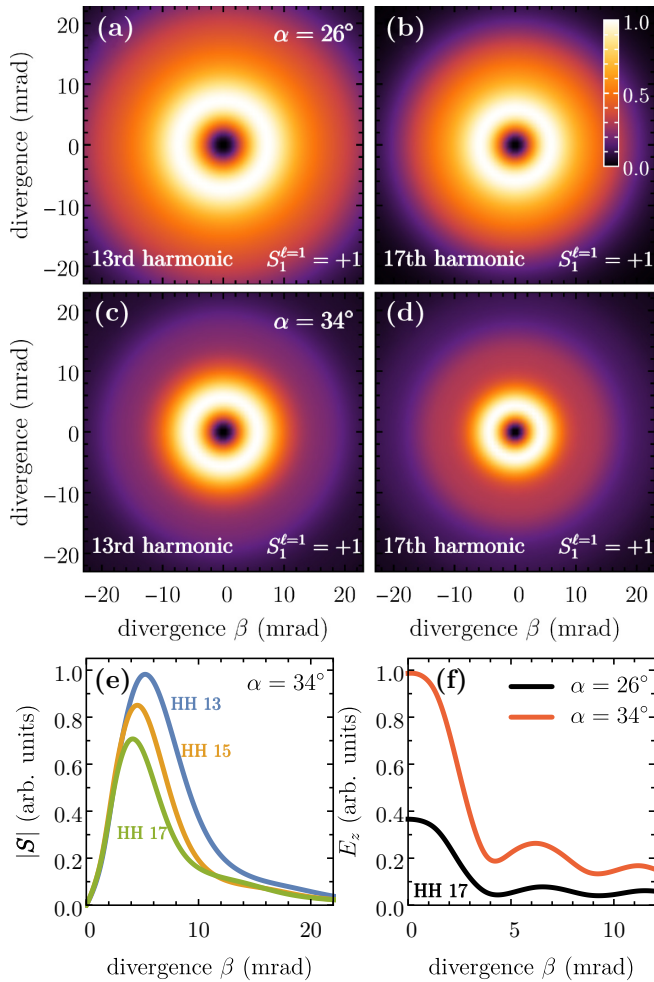


FIG. 2. (a)–(d) Angular intensity profiles showing the absolute value of the Poynting vector of two different harmonics (13 and 17) for two different laser focusings (upper row $\alpha = 26^\circ$; lower row $\alpha = 34^\circ$). (e) demonstrates the progress of divergency by increasing the harmonic order. (f) shows the longitudinal field of the 17th harmonic for two different focusing setups of the incident RVB. The quantity $S_1^{\ell=1} = +1$ corresponds to the extended Stokes parameter for cylindrical beams and reveals pure radial polarization [32].

exhibits a radial symmetry and a dark spot in the area around the optical axis, which can be explained by the diminishing intensity of the corresponding magnetic field when decreasing the axial distance. The polarization state is fully radial as inferred from calculating the extended (normalized) Stokes parameters $S_1^{\ell=1}$ for cylindrical beams [32]: Numerically, we found that $S_1^{\ell=1} = +1$ for all harmonics while the other two vanish. The influence of tightening the driving RVB focus is demonstrated in Figs. 2(c) and 2(d)]. It can be concluded that the intensity of the outer area decreases for a larger opening angle α . Figures 2(e) and 2(f) present the diffraction properties of the HHG process: Increasing the considered harmonic order, we find a tighter radiated beam spot since the axial distance to the intensity peak is lowered. However, the most exciting development is due to the longitudinal component of the emitted electric far field. As shown in Fig. 2(f), a sharper focus leads to a strongly pronounced on-axis field with

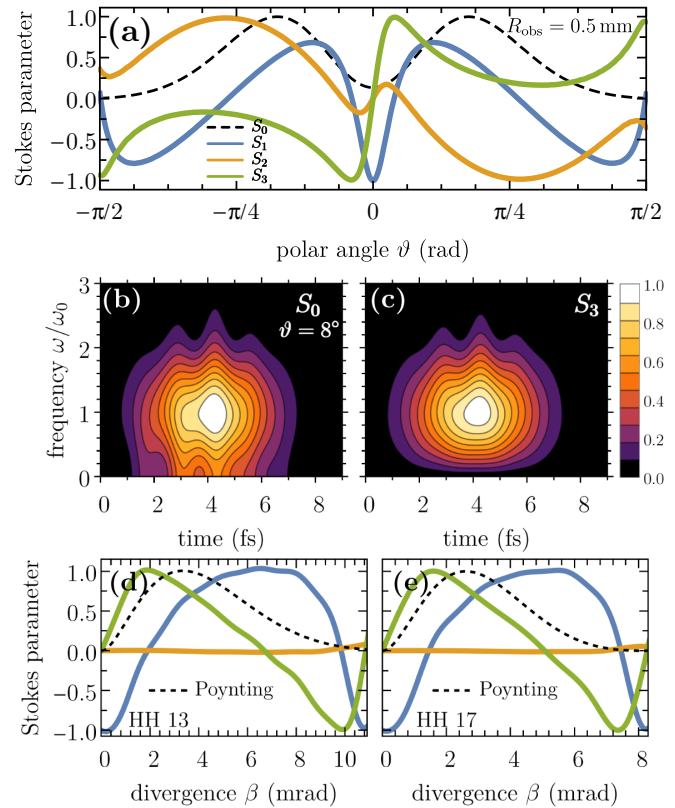


FIG. 3. Polarization landscape of emitted radiation for an incident RVB opening angle $\alpha = 30^\circ$. (a) Angular-dependent Stokes parameters of the electric first harmonic order at a sphere with radius $r_d = 0.5$ mm. (b), (c) Time-dependent spectrum and third Stokes parameter of the electric far field emitted in the asymptotic direction $\vartheta = 8^\circ$, recorded at $r_d = 0.5$ mm. (d), (e) (Normalized) Stokes parameters of the 13th and 17th harmonics as a function of divergence angle.

significant consequences for the polarization characteristics of the radiation. Figure 3 reveals the polarization structure of the emitted radiation, evidencing that the relation between the longitudinal and transverse field components of the driving field is transferred into the emitted higher-frequency fields. Due to cylindrical symmetry we confine the study of the polarization characteristics to the x - z plane. At first, we introduce the polar angle ϑ as the angle between the z axis and the asymptotic direction of the detector position r_d . In Fig. 3(a), we present the four Stokes parameters, evaluated for the radiated $E_x(r_d, t)$ and $E_z(r_d, t)$ as a function of the polar angle for an observer distance $r_d = 0.5$ mm. Noticeably, the polarization state changes continuously between linear (in z , $\pm 45^\circ$, and x directions) and circular. Due to symmetry, the radiation along the z axis can only be z polarized. A remarkable difference is the occurrence of the second Stokes parameter, which is absent in the incident RVB. Already at this stage, it is clear that (local) circular polarization can be observed in the far field as a result of the coherent superposition of the emission of the individual radiators. At $\vartheta = \pm 8^\circ$ we find highly distinctive circular polarization as evidenced by the (normalized) Stokes parameter $S_3 = 0.99$. The Stokes parameters nicely reflect the radial symmetry: The circular

polarization changes its sign since under $E_x(-\vartheta) = -E_x(\vartheta)$ while $E_z(-\vartheta) = E_z(\vartheta)$ which corresponds to a phase jump of π and reverses the direction. Hence, S_3 is an odd function. Note that $S_1 + S_2 + S_3 = S_0$, meaning the emission is fully polarized.

The time-dependent buildup of the Stokes parameters [33,34] (via a wavelet Fourier transform) are presented in Figs. 3(b) and 3(c). We choose the asymptotic direction of the radiation along $\theta = 8^\circ$ for an observer at the distance $r_d = 0.5$ mm (maximal degree of circular polarization). The time-dependent spectrum of the electric far field gives information about the duration of the emitted light pulse, which is in the fs regime. Furthermore, we find a symmetrical buildup and decay of the intensity (S_0) and the circular Stokes parameter (S_3). As already indicated in Fig. 3(a), S_0 and S_3 are virtually equal in the whole time frame, meaning that the radiation is always circularly polarized in this direction. We checked that S_1 and S_2 (not shown for brevity) are smaller than 0.05 at all times and frequencies, and hence the (circular) polarization degree is persistently >0.99 .

A key finding is the possibility to endow the higher-frequency regime with circular polarization, as shown in Figs. 3(e) and 3(f) for the spatially dependent Stokes parameters of the 13th and 17th harmonics for a varying divergence angle. In general, this behavior of S_1 , S_2 , and S_3 persists for higher-order harmonics in the (X)UV frequency regime. On axis, the harmonics are strict linearly polarized, characterized by $S_1 = -1$. The reason is the strong longitudinal component, which is discussed in Fig. 2. Increasing the axis distance results in the buildup of S_3 while S_1 decays. Reminiscent of the incident vector beam, as presented in Fig. 1(e), S_3 decays again while S_1 changes its sign and approaches unity. Hence, the polarization state changes from linear (in the z direction) to circular (relative to the x - z plane) to linear (in the x direction), meaning a transition into radial polarization when considering the whole beam spot. A high degree of ellipticity is around the maximum of the energy flux (Poynting vector), as indicated by the black dashed curve.

IV. MULTIPOLAR HHG

For insight into the polarity of the harmonics, we expand the electric far field in vector spherical harmonics on a sphere with radius r_{obs} ,

$$\mathbf{E}(\mathbf{r}_{\text{obs}}, t) = \sum_{L,M} a_{L,M}^{(r)}(t) \mathbf{Y}_{L,M} + a_{L,M}^{(1)}(t) \mathbf{\Psi}_{L,M} + a_{L,M}^{(2)}(t) \mathbf{\Phi}_{L,M}$$

(for conventions, cf. Ref. [35]). All harmonics are independent of the azimuthal angle φ due to symmetry. Therefore, all coefficients with $M \neq 0$ disappear (double checked numerically). As indicated by Fig. 4(a), for a small opening angle α , meaning a wide focusing, the transverse component $E_{\text{RVB}}^{(\rho)}$ of the incident RVB is dominating the light-matter interaction with the result that the irradiated atomic layer emits radiation characterized by even multipoles. For $n > 10$ we find harmonic orders where the quadrupole (e.g., $n = 13$ and 15) or even the hexadecapole (e.g., $n = 19$) are the leading multipole terms. The classical cutoff at $\hbar\omega_{\text{cutoff}} = 3.17U_{\text{pond}}$ (black arrow) is well reproduced as the harmonic yield decreases abruptly for $n > 30$.

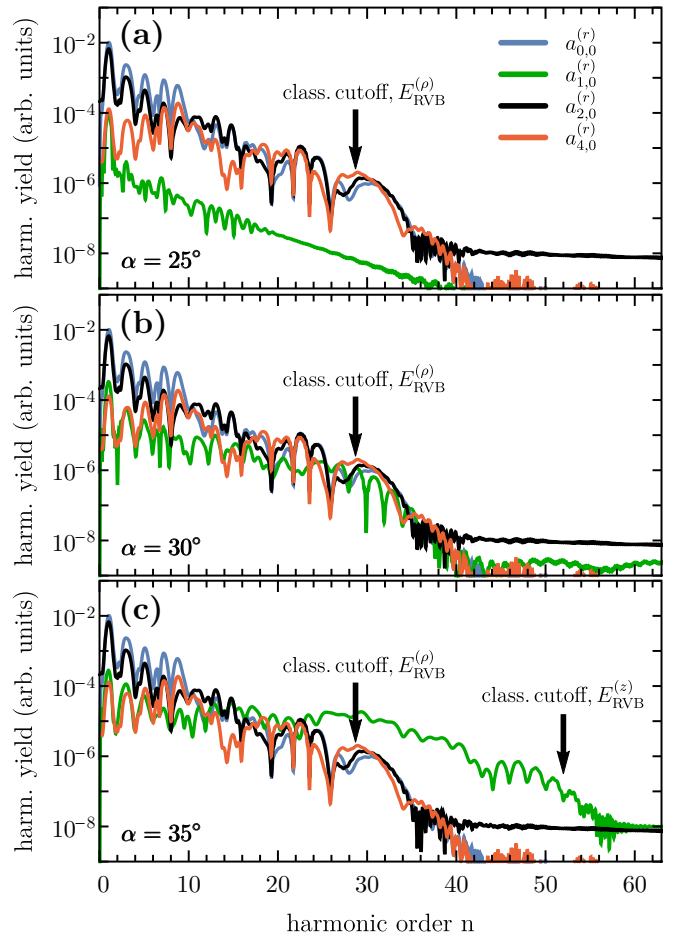


FIG. 4. Harmonic spectrum of the radiation produced by an incident RVB in dependence on the opening angle α . The angular momentum-dependent multipole coefficients $a_{L,0}^{(r)}$, as introduced in the text, characterize the multipolarity of the emitted harmonics of order n .

Note, atoms around the optical axis are exposed to $E_{\text{RVB}}^{(z)}$, and the dipole moment oscillates in the z direction. Thus, this part of the radiation is dominated by the dipolar coefficients as for conventional HHG. For the total HHG signal also the transverse component is decisive, which oscillates with a $\pi/2$ phase difference. Figure 4(b) evidences that a stronger focusing ($\alpha = 30^\circ$) boosts the dipole coefficient $a_{1,0}^{(r)}$ drastically to a level close to the even coefficients. An even stronger focusing ($\alpha = 35^\circ$ in which case $E_{\text{RVB}}^{(z)} > E_{\text{RVB}}^{(\rho)}$) has a substantial impact on the harmonic spectrum [Fig. 4(c)]: Although the lower-order harmonics ($n < 10$) are still dominated by the even multipole coefficients $a_{1,0}^{(r)}$, from $n > 15$ the harmonics are strongly dipolar. Moreover, the whole HH cutoff is shifted by more than 20 orders, which can be explained by the larger classical cutoff corresponding to the incident longitudinal component $E_{\text{RVB}}^{(z)}$. Astonishingly, we can produce (higher-order) harmonics with both parities by merely adjusting the waist of the driving pulse. The even multipole harmonics are a result of the radially polarized transverse electric-field component $E_{\text{RVB}}^{(\rho)}$ revealing mirror reflection symmetry. In contrast, the linearly polarized $E_{\text{RVB}}^{(z)}$ produces odd multipole

harmonics, comparable to conventional atomic HHG. A third unusual attribute is the shift of the cutoff frequency by focusing, provided the peak intensity of the RVB spot area is kept fixed.

HHG multipolarity is relevant to spectroscopy as, depending on polarity, HHs induce transitions with different propensity rules. The electric field of an emitted harmonic of order q can be expressed as

$$\mathbf{E}_q(\mathbf{r}, t) = \sum_L a_{L,0}^{(r),q}(\mathbf{r}) \mathbf{Y}_{LM} e^{-i\omega_q t}. \quad (1)$$

A numerical analysis of the radiated vector potential $\mathbf{A}(\mathbf{r}, t)$ reveals that it is approximately solenoidal. This is useful insofar as the coupling of $\mathbf{A}(\mathbf{r}, t)$ to the charge current density of a finite-size sample can be unitarily transformed to the following form (\mathbf{r}_j is the position of the electron),

$$\hat{H}_{\text{int}}^q(t) = H_{\text{int}} e^{-i\omega_q t} = \sum_{L,j} a_{L,0}^{(r),q}(\mathbf{r}_j) (\mathbf{r}_j \cdot \mathbf{Y}_{L,0}) e^{-i\omega_q t}. \quad (2)$$

For a demonstration, let us consider an isotropic system amenable to an effective single-particle description. The ground-state single-particle orbital can thus be written as $\Psi_i(\mathbf{r}, t) = R_i(r) Y_{0,0}(\Omega_r)$ with orbital energy E_i . A transition to an excited state, presented by

$$\Psi_f(\mathbf{r}, t) = R_f(r) Y_{\ell_f,0}(\Omega_r)$$

with orbital energy E_f , is governed by the matrix element

$$\begin{aligned} \langle \Psi_f | H_{\text{int}} | \Psi_i \rangle &\propto \frac{1}{\sqrt{4\pi}} \sum_{\ell_f} \sum_L \sqrt{(2\ell_f + 1)(2L + 1)} \\ &\times \mathcal{A}_{\ell_f, L} \begin{pmatrix} \ell_f & L & 0 \\ 0 & 0 & 0 \end{pmatrix}^2, \end{aligned} \quad (3)$$

where

$$\mathcal{A}_{\ell_f, L} = \int_0^\infty dr r^3 a_{L,0}^{(r),q}(\mathbf{r}) R_f(r) R_i(r).$$

The final orbital angular momentum quantum number ℓ_f fulfills the condition $\ell_f = L$. As a consequence, the leading multipole coefficient $a_{L,0}^q$ characterizes the atomic transition. Considering the result presented in Fig. 4(c), the electric fields of the lower HHs (harmonic order $n < 15$) would initiate an even multipole transition ($n_i s \rightarrow n_f s$ or $n_i s \rightarrow n_f d$). Choosing instead higher-order harmonics ($n > 20$) would result in dipole transitions, i.e., $n_i s \rightarrow n_f p$.

V. CONCLUSIONS

HHG by focused radially polarized vector fields is dominated by the interplay between the longitudinal and the transversal laser components which oscillate with a $\pi/2$ phase difference and amplitudes that depend on focusing. Extreme focusing poses a challenge to experiments as the gradient of the longitudinal component along the optical axis becomes steeper. However, the predicted effects are strongest when the longitudinal and transversal components are of comparable strengths. In addition, when averaging over the atom distributions the atoms right on the optical axis have a smaller weight. Harmonics akin to RVB exhibit a local circular polarization *perpendicular* to the focal plane, meaning

that circular polarized HHGs are producible and tunable by varying the beam waist. The discussed circular polarization relates to the transverse spin angular momentum, discussed Ref. [36]. Furthermore, multipolar, even, and odd harmonics are generated. The predicted effects highlight the potential of using structured laser pulses with inherent longitudinal field components for nonlinear processes in matter.

ACKNOWLEDGMENT

This research is funded by the Deutsche Forschungsgemeinschaft (DFG) under SFB TRR227, SPP1840, and WA 4352/2-1.

APPENDIX: DESCRIPTION VIA LG MODES

The vector potential of a Laguerre-Gaussian (LG) mode with $|m| = 1$ and $p = 0$ is given in cylindrical coordinates $\mathbf{r} = \{\rho, \varphi, z\}$ by [37]

$$\begin{aligned} \mathbf{A}_{\text{LG}}^{m,\sigma}(\mathbf{r}, t) &= \hat{e}_\sigma A_0 \mathcal{N}_{\text{LG}} \frac{w_0}{w(z)} \frac{\sqrt{2}\rho}{w(z)} e^{-\frac{\rho^2}{w^2(z)}} \\ &\times e^{i\frac{q\rho^2}{2R(z)} + im\varphi + i\zeta(z)} e^{i(qz - \omega t)} + \text{c.c.} \end{aligned} \quad (A1)$$

Here, σ indicates the polarization state with the corresponding vector $\hat{e}_\sigma = e^{i\sigma\varphi} (1, i\sigma, 0)^T / \sqrt{2}$. The beam width is $w(z) = w_0 \sqrt{1 + (z/z_R)^2}$, where w_0 is the beam waist while $z_R = qw_0^2$ is the Rayleigh length for a wave number $q = \omega/c$. The function $R(z)$ is the wave-front radius of curvature, given by $R(z) = z[1 + (z_R/z)^2]$, and $\zeta(z) = -2 \tan^{-1}(z/z_R)$ is the Gouy phase. The normalization constant $\mathcal{N}_{\text{LG}} = \sqrt{2}e$ was chosen in a way that $\mathbf{A}_{\text{LG}}^{m,\sigma}(\rho_{\text{max}}, z, t) = A_0$, where at ρ_{max} the peak amplitude can be found.

The vector potential of a radial vector beam (RVB) can be found by a sum of $\mathbf{A}_{\text{LG}}^{+1,-1}(\mathbf{r}, t)$ and $\mathbf{A}_{\text{LG}}^{-1,+1}(\mathbf{r}, t)$ yielding

$$\begin{aligned} \mathbf{A}_{\text{LG}}^{\text{RVB}}(\mathbf{r}, t) &= A_0 \mathcal{N}_{\text{LG}} \frac{w_0}{w(z)} \frac{\rho}{w(z)} e^{-\frac{\rho^2}{w^2(z)}} \\ &\times e^{i\frac{q\rho^2}{2R(z)} + i\zeta(z)} e^{i(qz - \omega t)} \hat{e}_\rho + \text{c.c.} \end{aligned} \quad (A2)$$

The vector potential is not solenoidal, i.e., via the Lorenz gauge condition $\nabla \cdot \mathbf{A}_{\text{LG}}^{\text{RVB}} + \partial_t \Phi_{\text{LG}}^{\text{RVB}}/c^2 = 0$ it gives rise to an electromagnetic scalar potential,

$$\begin{aligned} \Phi_{\text{LG}}^{\text{RVB}}(\mathbf{r}, t) &= A_0 \mathcal{N}_{\text{LG}} \frac{\omega}{q^2} \frac{w_0}{R(z)w^4(z)} e^{-\frac{\rho^2}{w^2(z)}} e^{i\frac{q\rho^2}{2R(z)} + i\zeta(z)} \\ &\times [q\rho^2 w^2(z) + 2iR(z)(\rho^2 - w^2(z))] \\ &\times e^{i(qz - \omega t)} + \text{c.c.} \end{aligned} \quad (A3)$$

Finally, the associated electric field can be found by $\mathbf{E}_{\text{LG}}^{\text{RVB}}(\mathbf{r}, t) = -\partial_t \mathbf{A}_{\text{LG}}^{\text{RVB}}(\mathbf{r}, t) - \nabla \Phi_{\text{LG}}^{\text{RVB}}(\mathbf{r}, t)$, resulting in both a transversal *and* longitudinal field component. The electric field in the plane $z = 0$ reads explicitly

$$\begin{aligned} E_{\text{LG},\rho}^{\text{RVB}} &= E_0 \mathcal{N}_{\text{LG}} \frac{\rho}{q^2 w_0^5} e^{-\frac{\rho^2}{w_0^2}} [4\rho^2 - 8w_0^2 + q^2 w_0^4] \sin(\omega t), \\ E_{\text{LG},\varphi}^{\text{RVB}} &= 0, \\ E_{\text{LG},z}^{\text{RVB}} &= 2E_0 \mathcal{N}_{\text{LG}} \frac{1}{q^3 w_0^7} e^{-\frac{\rho^2}{w_0^2}} \cos(\omega t) \\ &\times [2\rho^4 + 4w_0^4 - q^2 w_0^6 + \rho^2 w_0^2 (q^2 w_0^2 - 8)]. \end{aligned} \quad (A4)$$

where $E_0 = A_0 \omega$.

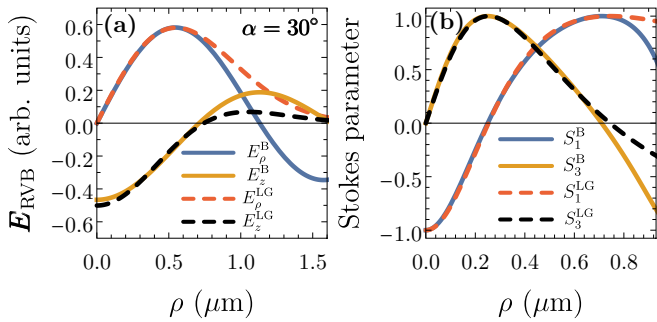


FIG. 5. Comparison between RVBs constructed out of Bessel (B) modes and LG modes. (a) Transversal and longitudinal fields in dependence on the axial distance ρ . (b) Spatially dependent (normalized) Stokes parameters S_1 and S_3 . The opening angle of $\alpha = 30^\circ$ belongs to an LG waist size of $w_0 = 0.72 \mu\text{m}$.

In Fig. 5 we show a comparison between the RVB electric fields constructed out of Bessel modes [Fig. 5(a)] and LG

modes [Fig. 5(b)] in a focused condition, i.e., $\alpha = 30^\circ$, which corresponds to an LG waist $w_0 = 0.72 \mu\text{m}$. As presented in Fig. 5(a), the longitudinal and transversal components show similar trends. While near the optical axis the agreement is remarkable, larger deviations occur behind the first intensity maxima. The reason is the exponentially decreasing field amplitude of the LG mode, while the Bessel beam exhibits infinity side maxima.

The Stokes parameters in the ρ - z plane of the driving field are important, shown in Fig. 5(b). Here, LG and Bessel RVBs show a remarkable agreement: The zone around the optical axis is (z) linearly polarized (Stokes parameter $S_1 \cong -1$), while increasing the axial distance yields a region with a pronounced circular polarization ($S_3 \cong +1$). Increasing ρ further results in in-plane polarization (Stokes parameter $S_1 \cong +1$), which means the beam is radially polarized in this region. Similar to Fig. 5(a), LG and Bessel Stokes parameters start to deviate for $\rho > 0.8 \mu\text{m}$. Since we consider a small interaction volume with an effective radius of $1 \mu\text{m}$, we expect similar results as reported in Figs. 2–4 when using LG modes instead of Bessel modes for the construction of the RVB.

[1] P. Agostini and L. F. DiMauro, *Rep. Prog. Phys.* **67**, 813 (2004).
 [2] F. Krausz and M. Ivanov, *Rev. Mod. Phys.* **81**, 163 (2009).
 [3] T. Popmintchev, M.-C. Chen, P. Arpin, M. M. Murnane, and H. C. Kapteyn, *Nat. Photonics* **4**, 822 (2010).
 [4] Y. Toda, S. Honda, and R. Morita, *Opt. Express* **18**, 17796 (2010).
 [5] M. Zürrich, C. Kern, P. Hansinger, A. Dreischuh, and C. Spielmann, *Nat. Phys.* **8**, 743 (2012).
 [6] C. Hernández-García, A. Picón, J. San Román, and L. Plaja, *Phys. Rev. Lett.* **111**, 083602 (2013).
 [7] G. Garipey, J. Leach, K. T. Kim, T. J. Hammond, E. Frumker, R. W. Boyd, and P. B. Corkum, *Phys. Rev. Lett.* **113**, 153901 (2014).
 [8] R. Géneaux, A. Camper, T. Auguste, O. Gobert, J. Caillat, R. Taïeb, and T. Ruchon, *Nat. Commun.* **7**, 12583 (2016).
 [9] C. Hernández-García, A. Turpin, J. San Román, A. Picón, R. Drevinskas, A. Cerkauskaitė, P. G. Kazansky, C. G. Durfee, and Í. J. Sola, *Optica* **4**, 520 (2017).
 [10] J. Wätzel and J. Berakdar, *Opt. Express* **25**, 27857 (2017).
 [11] W. Paufler, B. Böning, and S. Fritzsche, *J. Opt.* **21**, 094001 (2019).
 [12] L. Rego, K. M. Dorney, N. J. Brooks, Q. L. Nguyen, C.-T. Liao, J. San Román, D. E. Couch, A. Liu, E. Pisanty, M. Lewenstein *et al.*, *Science* **364**, 9486 (2019).
 [13] W. Chao, B. D. Harteneck, J. A. Liddle, E. H. Anderson, and D. T. Attwood, *Nature (London)* **435**, 1210 (2005).
 [14] J. Miao, T. Ishikawa, I. K. Robinson, and M. M. Murnane, *Science* **348**, 530 (2015).
 [15] C. Wagner and N. Harned, *Nat. Photonics* **4**, 24 (2010).
 [16] G. Tallents, E. Wagenaars, and G. Pert, *Nat. Photonics* **4**, 809 (2010).
 [17] Q. Zhan, *Adv. Opt. Photonics* **1**, 1 (2009).
 [18] J. Lin, Y. Ma, P. Jin, G. Davies, and J. Tan, *Opt. Express* **21**, 13193 (2013).
 [19] J. Wätzel, C. M. Granados-Castro, and J. Berakdar, *Phys. Rev. B* **99**, 085425 (2019).
 [20] D. D. Hickstein, F. J. Dollar, P. Grychtol, J. L. Ellis, R. Knut, C. Hernández-García, D. Zusin, C. Gentry, J. M. Shaw, T. Fan *et al.*, *Nat. Photonics* **9**, 743 (2015).
 [21] C. Chen, Z. Tao, C. Hernández-García, P. Matyba, A. Carr, R. Knut, O. Kfir, D. Zusin, C. Gentry, P. Grychtol *et al.*, *Sci. Adv.* **2**, e1501333 (2016).
 [22] A. Fleischer, O. Kfir, T. Diskin, P. Sidorenko, and O. Cohen, *Nat. Photonics* **8**, 543 (2014).
 [23] P.-C. Huang, C. Hernández-García, J.-T. Huang, P.-Y. Huang, C.-H. Lu, L. Rego, D. D. Hickstein, J. L. Ellis, A. Jaron-Becker, A. Becker *et al.*, *Nat. Photonics* **12**, 349 (2018).
 [24] M. Nurhuda and F. H. M. Faisal, *Phys. Rev. A* **60**, 3125 (1999).
 [25] D. J. Griffiths and D. F. Schroeter, *Introduction to Quantum Mechanics* (Cambridge University Press, Cambridge, UK, 2018).
 [26] O. D. Jefimenko, *Electricity and Magnetism: An Introduction to the Theory of Electric and Magnetic Fields* (Electret Scientific Company, 1989).
 [27] C. Hernández-García, J. A. Pérez-Hernández, J. Ramos, E. C. Jarque, L. Roso, and L. Plaja, *Phys. Rev. A* **82**, 033432 (2010).
 [28] C. Hernández-García, Coherent attosecond light sources based on high-order harmonic generation: Influence of the propagation effects, Ph.D. thesis, Universidad de Salamanca, 2013.
 [29] C. Hernández-García, W. Holgado, L. Plaja, B. Alonso, F. Silva, M. Miranda, H. Crespo, and I. J. Sola, *Opt. Express* **23**, 21497 (2015).
 [30] W. H. McMaster, *Am. J. Phys.* **22**, 351 (1954).
 [31] Z.-P. Zhuang, R. Chen, Z.-B. Fan, X.-N. Pang, and J.-W. Dong, *Nanophotonics* **8**, 1279 (2019).

- [32] M. Suzuki, K. Yamane, K. Oka, Y. Toda, and R. Morita, *Opt. Rev.* **22**, 179 (2015).
- [33] J. Eberly and K. Wodkiewicz, *J. Opt. Soc. Am.* **67**, 1252 (1977).
- [34] A. S. Moskalenko, Z.-G. Zhu, and J. Berakdar, *Phys. Rep.* **672**, 1 (2017).
- [35] R. G. Barrera, G. Estevez, and J. Giraldo, *Eur. J. Phys.* **6**, 287 (1985).
- [36] A. Aiello, P. Banzer, M. Neugebauer, and G. Leuchs, *Nat. Photonics* **9**, 789 (2015).
- [37] L. Allen, M. W. Beijersbergen, R. J. C. Spreeuw, and J. P. Woerdman, *Phys. Rev. A* **45**, 8185 (1992).